



The flower-like BiOCl/BiOBr with heterojunction prepared by co-precipitation method to enhance its photocatalytic performance

Yeheng Zhang¹, Wensong Lin^{1,a)} , Ran Gao¹, Huanxia Lin¹, Yong He¹

¹ School of Materials Science and Engineering, Shanghai University of Engineering Science, Shanghai 201620, People's Republic of China

^{a)} Address all correspondence to this author. e-mail: wslin@sues.edu.cn

Received: 25 October 2023; accepted: 5 March 2024; published online: 15 March 2024

One-step co-precipitation method was used to prepare the flower-like BiOCl/BiOBr composite materials (BOBCs) with heterojunction structures, in which various amounts of BiOBr were used to adjust the band gap of BiOCl and thereby improve its photocatalytic activity. Based on photocatalytic performance experiments, BOBC2, in which the molar ratio of BiOCl to BiOBr is 1:0.75, exhibited the highest photodegradation efficiency (90.5%) to remove ofloxacin after 100 min illumination. The cyclic utilization performance of BOBC2 under the same conditions was tested by a cycle experiment. It was found that its photocatalytic activity remained at a high level after three cycles. The composition and microstructure of the material were analyzed by characterization techniques including XRD, FTIR, XPS, and SEM. The optical properties and the degradation process of the material were studied by DRS, PL, photocurrent, and active species trapping methods. The reasonable mechanism for photocatalytic degradation of ofloxacin was proposed.

Introduction

Ofloxacin as one kind of antibiotics [1], having been widely used in the field to treat bacterial infections in humans or other animals because it can inhibit or eliminate various common bacteria. With the wide application of antibiotics in many fields, a large amount of ofloxacin is discharged into our daily environment with the sewage generated by hospitals, pharmaceutical factories and animal husbandry [1–3]. These ofloxacin residues in sewage are difficult to remove [4, 5], leading to some bacteria resistance to ofloxacin or accumulation in the human body through the biological chain [6]. Due to the characteristics of ofloxacin, conventional physical or chemical methods such as precipitation, coagulation, neutralization, adsorption and other treatment methods can not completely remove ofloxacin in aqueous solution, and may cause secondary pollution [7, 8]. Therefore, it become urgent and significant to find an energy-saving treatment technology to remove ofloxacin. In recent years, photocatalytic technology has gradually entered the research field of photocatalysis for its ability to effectively treat harmful organic pollutants in wastewater [9–11]. Previous experimental studies have shown that the photogenerated

electron–hole pairs generated by some semiconductor materials when excited by external light sources can cause reduction or oxidation reactions of organic pollutants in water [12, 13], effectively degrading most organic dyes, antibiotics, and other organic pollutants in the environment.

In photocatalytic semiconductor materials, bismuth halide oxides (BiOX, X = Cl, Br, and I) [14] with unique layered structure have been considered to be great potential for application in the field of photocatalysis owing to their suitable bandgap, and non-toxic and inexpensive properties. Among them, the tetragonal structure of BiOCl consists of [Cl–Bi–O–Bi–Cl] [15] covalent bond layers, which are superposed and kept together by the Van der Waals force interaction between halides. For this special structure, the relevant atoms and orbitals have sufficient polarization space, which can promote the separation of photo-generated charge carriers [16]. According to existing studies, BiOCl catalysts exhibit high photocatalytic activity, but their wide bandgap (E_g approximately 3–3.6 eV) limits the separation rate of photo-generated carriers, made their practical photocatalytic activity worsen [17]. In order to decrease the recombination rate of photogenerated carriers in BiOCl, methods to

modifying BiOCl have been developed by researchers. Overall, there are three common methods to enhance the photocatalytic efficiency of BiOCl photocatalytic materials: controlling the microstructure of BiOCl, ion doping of BiOCl materials [18], and constructing heterostructures with other semiconductors [19].

The construction of heterojunctions [20] can enhance the separation efficiency of photo-generated carriers by forming an interface electric field, which is an effective method to improve photocatalytic performance. In recent years, some researchers have combined bismuth halides composed of different halogens to construct heterostructures [21], such as BiOCl/BiOBr [22], BiOBr/BiOI [23], and BiOCl/BiOI [21], in order to increase the separation rate of photo-generated carriers. Compared to heterostructures composed of BiOX and other materials, the BiOX/BiOY heterostructure demonstrates a robust configuration. Furthermore, by manipulating the compositions of BiOX and BiOY, it is feasible to finely tune its inherent optical properties [24] and oxidation potential. This feature holds promise for academic applications, highlighting its structural stability and controllable physicochemical characteristics [25]. Zhang et al. [24] synthesized BiOCl/BiOBr microspheres by a hydrothermal process, and Liao et al. [26] constructed flower shaped BiOCl/BiOBr in aqueous solution containing acetic acid. Both results gotten by them have proved that the degradation of Rhodamine B by BiOCl/BiOBr composite photocatalyst materials has been significantly improved. Liu et al. [27] synthesized layered BiOCl/BiOBr using ultrasonic and precipitation method in aqueous solution with ethanol under UV induction, which improved the photocatalytic performance of the material. These studies mainly focus on the degradation of organic dyes by bismuth halide oxide composite materials.

Inspired by the above reports, this article adopts a one-step precipitation method to synthesize BiOCl composites with various compositions of BiOBr under acidic conditions. The relationship between the process parameters and the photocatalytic performance of BiOCl/BiOBr composites was assessed by photocatalytic degradation of ofloxacin. The BiOCl/BiOBr photocatalytic materials were characterized by XRD, FTIR, XPS, SEM, BET, UV-Vis diffuse reflectance, and other methods. The photocatalytic degradation mechanism of ofloxacin under visible-light irradiation by BiOCl/BiOBr was analyzed through free radical capture and ESR experiments.

Results and discussion

Compositional and structural information

Figure 1 showed the XRD spectra of pure BiOCl, BiOBr, and three BOBCs. It is evident that the diffraction peaks at 11.9° , 25.8° , 32.6° , 33.4° , 46.8° , 54.2° , and 58.7° of BiOCl sample

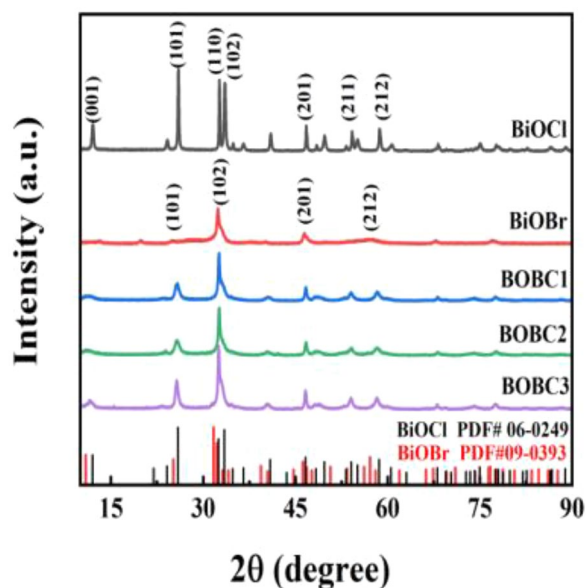


Figure 1: XRD patterns of different photocatalysts.

are consistent with the standard PDF card (JCPDS 06-0249), corresponding to (001), (101), (110), (102), (201), (211), and (212) crystal planes of BiOCl [28], respectively. The diffraction peaks at 25.3° , 32.4° , 46.5° , and 57.2° of BiOBr sample are consistent with the standard PDF card (JCPDS 09-0393), corresponding to (101), (102), (201), and (211) crystal planes of BiOBr [29], respectively. The diffraction peaks appeared in the BOBC1, BOBC2, and BOBC3 samples are all aligned to the characteristic peaks of BiOCl or BiOBr, and no other diffraction peaks were detected, indicating that the three BOBCs are all only composed of BiOCl and BiOBr.

The functional groups of BiOCl, BiOBr and BOBC2 were characterized in the FTIR spectra. As demonstrated in the Fig. 2, the vibration peak at 520 cm^{-1} , 1400 cm^{-1} , 1630 cm^{-1} and 3440 cm^{-1} are attributed to the Bi-O [30] stretching vibration, Bi-Cl or Bi-Br in BiOCl or BiOBr [31, 32], and hydroxyl stretching vibration caused by water absorption [33], respectively. There are no other vibration peaks in the FTIR spectra were found, further proving the successful synthesis of BiOCl/BiOBr composite materials.

The elemental composition and chemical states of the surface of pure BiOCl, pure BiOBr, and BOBC2 samples were studied by XPS. As demonstrated in the [Fig. 3(a)], the full XPS spectra revealed the existence of C, Bi, O, Cl or/and Br in pure BiOCl, BiOBr, and BOBC2 samples. The carbon element should be attributed to the amorphous carbon of the sample [34]. The high-resolution XPS spectra of Bi 4f [21] were shown [Fig. 3(b)]. The peaks in the spectra revealed the binding energy of 158.7 eV and 164 eV in BiOCl, 158.1 eV and 163.5 eV in BiOBr, 158.5 eV and 163.8 eV in BOBC2,

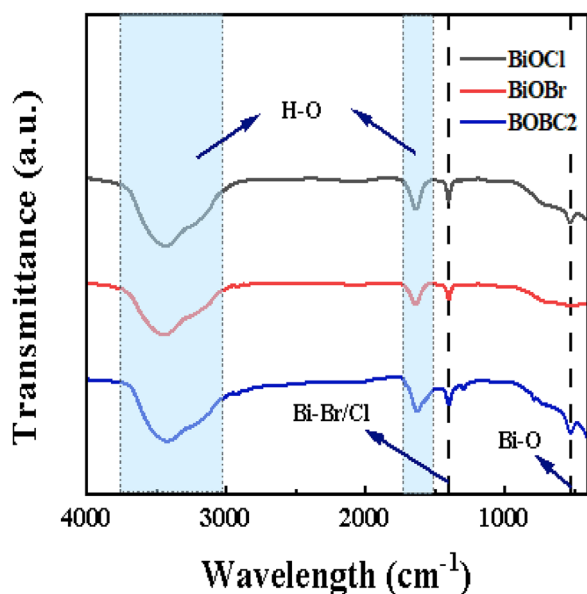


Figure 2: FTIR spectra of BiOCl, BiOBr, and BOBC2.

respectively, which all were in consistence with the peaks of Bi $4f_{7/2}$ and $4f_{5/2}$, indicating that Bi^{3+} exists in the pure BiOCl, BiOBr and BOBC2 samples. Compared with pure BiOCl and BiOBr, the binding energies of Bi $4f_{7/2}$ and $4f_{5/2}$ in BOBC2 have a blue-shift and a red-shift, respectively, which can be attributed to the interaction between BiOCl and BiOBr.

A high-resolution XPS spectra of Cl $2p_{3/2}$ and Cl $2p_{1/2}$ were shown in [Fig. 3(c)]. The peaks at 197.4 and 199 eV were appeared in BiOCl, and the peaks at 197 and 198.8 eV were found in BOBC2 [35]. We can find that the peaks of Cl $2p$ in BOBC2 were blue shifted compared with those in pure BiOCl, indicating that the orbit of Cl $2p$ in BiOCl was occupied by extra photogenerated electrons. Figure 3(d) showed the high-resolution XPS spectra of Br $3d_{5/2}$ and Br $3d_{3/2}$. The peaks at 67.3 eV and 68.4 eV, and 67.7 eV and 68.8 eV were appeared in BiOBr and BOBC2, respectively [36]. Red shifted can be found in the peaks of Br $3d$ in pure BiOBr as compared with those of BOBC2, which can be attributed to some electrons in the orbit of Br $3d$ in BiOBr are lost during the irradiation process [37]. From the above data, it can be concluded that electrons migrate from the BiOBr interface to BiOCl in BOBC2, forming an internal electric field.

Figure 3(e) showed the high-resolution spectra of O $1s$ of BiOCl, BiOBr and BOBC2. The peaks appeared at 529.4 and 531 eV in BiOCl, 529.2 and 530.8 eV in BiOBr, and 528.9 and 530.5 eV in BOBC2, are all attributed to lattice oxygen and hydroxyl in above substances [38].

The results measured by XRD, FTIR, and XPS methods confirmed the presence of BiOCl and BiOBr in BOBCs,

suggesting the successful synthesis of heterostructures existing in BiOCl/BiOBr.

Microstructure information

The SEM images of BiOBr, BiOCl, and BOBC2 materials were shown in [Fig. 4(a–d)]. As indicated in [Fig. 4(a)], the large amount of stacked nanosheets with side length of 100–600 nm and thickness of about 20 nm can be easily observed in BiOBr. The BiOBr shows the flower-like structure in [Fig. 4(b)]. Figure 4(c and d) show the morphology of the BOBC2 composite material at different magnifications. It can be seen clearly that BOBC2 exhibits a uniform flower-like structure assembled with nanosheets. Contrasted with the stacked lamellar structure, the flower-like structure enhances the specific surface area, thus enhancing more active site and improving the photocatalytic activity. The EDS in [Fig. 4(e)] shows the presence of Bi, O, Cl, and Br uniformly distributed in BOBC2, suggesting the successful combination of BiOCl with BiOBr.

Figure 5 displays the nitrogen adsorption–desorption isotherms for BiOCl, BiOBr and BOBC2. At relatively high relative pressures, distinct hysteresis loops, indicating typical type IV isotherms [39], can be observed in the curves, suggesting that BiOCl, BiOBr, and BOBC2 are all mesoporous materials. By measuring the nitrogen adsorption–desorption isotherms, the calculated surface areas [40] of BiOCl, BiOBr, and BOBC2 were $9.0591 \text{ m}^2 \text{ g}^{-1}$, $15.243 \text{ m}^2 \text{ g}^{-1}$, and $24.471 \text{ m}^2 \text{ g}^{-1}$, respectively. Similarly, using the Barrett–Joyner–Halenda (BJH) desorption method, the pore volumes of BiOCl, BiOBr, and BOBC2 were calculated as $0.0317 \text{ cm}^3 \text{ g}^{-1}$, $0.0662 \text{ cm}^3 \text{ g}^{-1}$, and $0.1071 \text{ cm}^3 \text{ g}^{-1}$, respectively. The BET surface area and pore volume information for BiOCl, BiOBr, and BOBC2 are outlined in Table 1. The findings indicate that the incorporation of BiOBr increased both the specific surface area and pore volume of BOBC2, leading to a higher amount of adsorption and active sites, thereby enhancing the photocatalytic performance of the material.

Optical and electronic properties

UV–visible diffuse reflection spectroscopy (DRS) was used to investigate the optical properties of pure BiOCl, BiOBr, and BOBC materials. As demonstrated in the [Fig. 6(a)], the absorption edges of pure BiOCl and BiOBr were located at 360 and 408 nm, respectively, while the absorption edge of BOBC was in the range of 380–400 nm. The addition of BiOBr in BiOCl led to a redshift in the absorption edge of the composite material, resulting in a stronger absorption capacity for visible-light.

Generally, the Kubelka–Munk function (Eq. 1) [39] is used to calculate the bandgap width of materials:

$$\alpha h\nu = A \cdot (h\nu - E_g)^{n/2} \quad (1)$$

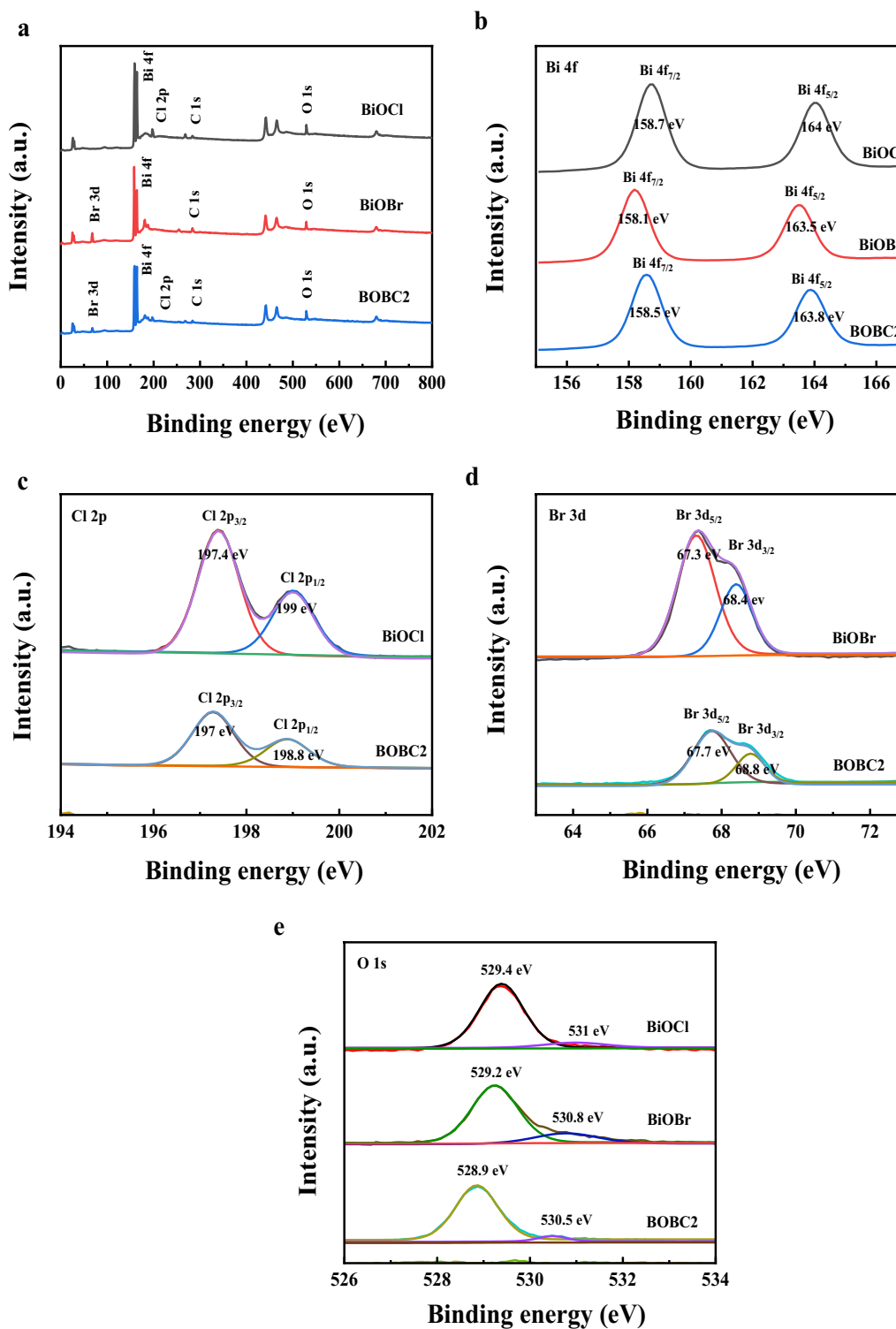


Figure 3: XPS spectra: (a) full spectra of BiOCl, BiOBr, and BOBC2. (b) Bi 4f of BiOCl, BiOBr, and BOBC2. (c) Cl 2p of BiOCl and BOBC2. (d) Br 3d of BiOBr and BOBC2. (e) O 1s of BiOCl, BiOBr, and BOBC2.

where α , h , ν , and E_g represent the absorption coefficient, Planck's constant, photonic frequency, and energy band gap, respectively. A is a constant, and the value of the exponent n depends on the type of semiconductor ($n=1$ for direct

transitions, $n=4$ for indirect transitions). According to literature reports, BiOX is an indirect bandgap semiconductor with $n=4$. [25] From this, the calculated bandgap energy (E_g) values for BiOCl, BiOBr, and BOBC2 are 3.23 eV, 2.84 eV, and 2.93 eV,

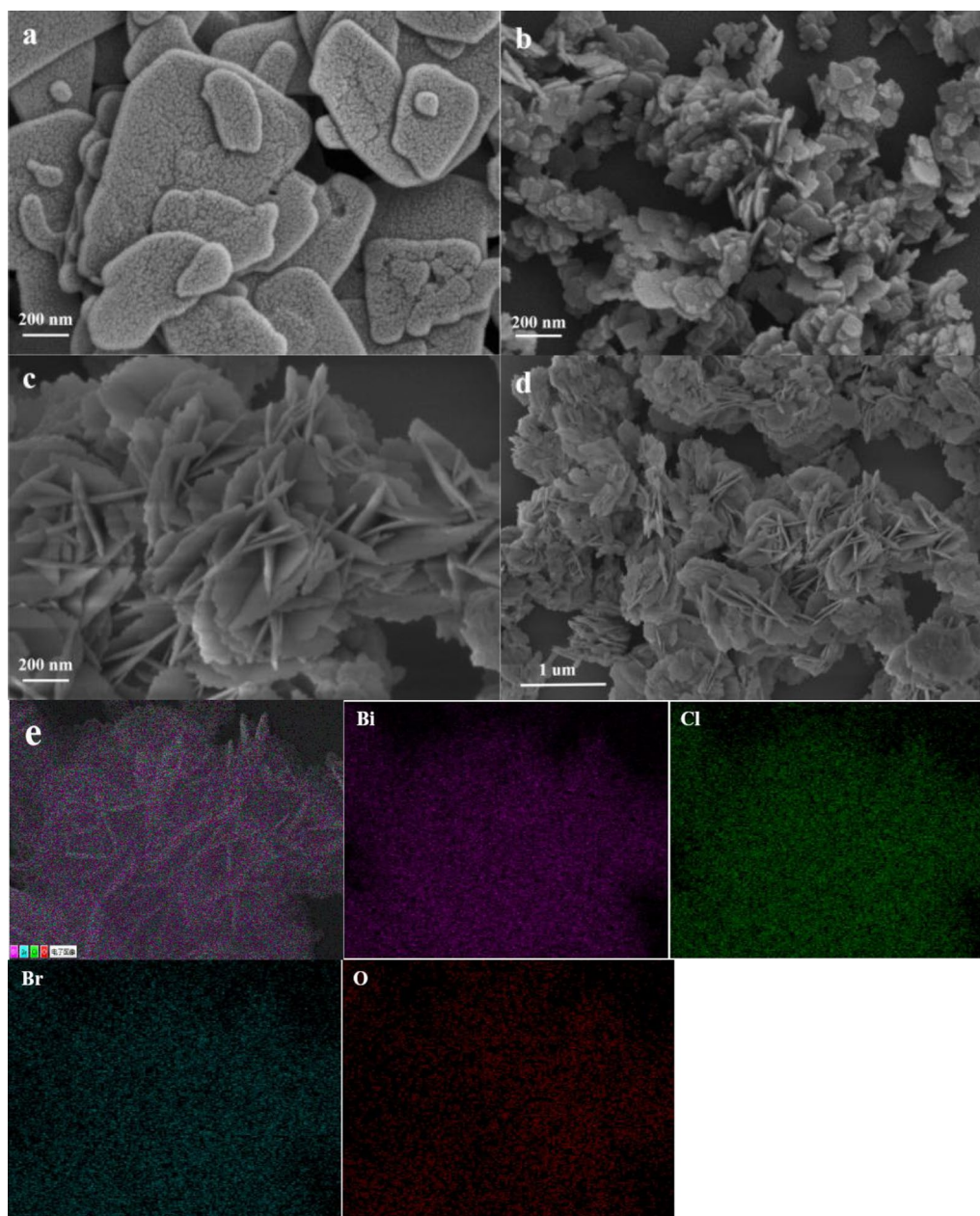


Figure 4: SEM morphologies of pure BiOCl (a), BiOBr (b) and BOBC2 (c, d) and EDS mapping of BOBC2 (e).

respectively. The addition of BiOBr results in a smaller bandgap for the composite material compared with BiOCl.

The conduction band potential (CB) and valence band potential (VB) of BiOCl and BiOBr can be calculated using the Mulliken electronegativity theory (Eqs. 2 and 3): [41]

$$E_{VB} = X - E_e + 0.5E_g \quad (2)$$

$$E_{CB} = E_{VB} - E_g \quad (3)$$

where X is the geometric mean of the electronegativity of the constituent atoms ($X_{\text{BiOCl}} = 6.36$ eV, $X_{\text{BiOBr}} = 6.17$ eV), [42] E_e is the free electron energy on the hydrogen scale (usually

$E_e = 4.5$ eV), and E_g is the bandgap potential. By calculations, VB of BiOCl and BiOBr is found to be 3.47 and 3.10 eV, respectively, while CB of them is 0.24 and 0.23 eV, respectively.

Photoluminescence (PL) spectroscopy employing an excitation wavelength of 270 nm was employed to investigate the charge carrier separation, transfer, and recombination capabilities of the BOBCs materials during photocatalytic reactions [43]. As demonstrated in [Fig. 7(a)], the emission peaks of BiOCl, BiOBr, and BOBC materials were mainly concentrated at 540 nm. The order of luminescence intensity for the photocatalysts was BiOCl > BiOBr > BOBC1 > BOBC3 >

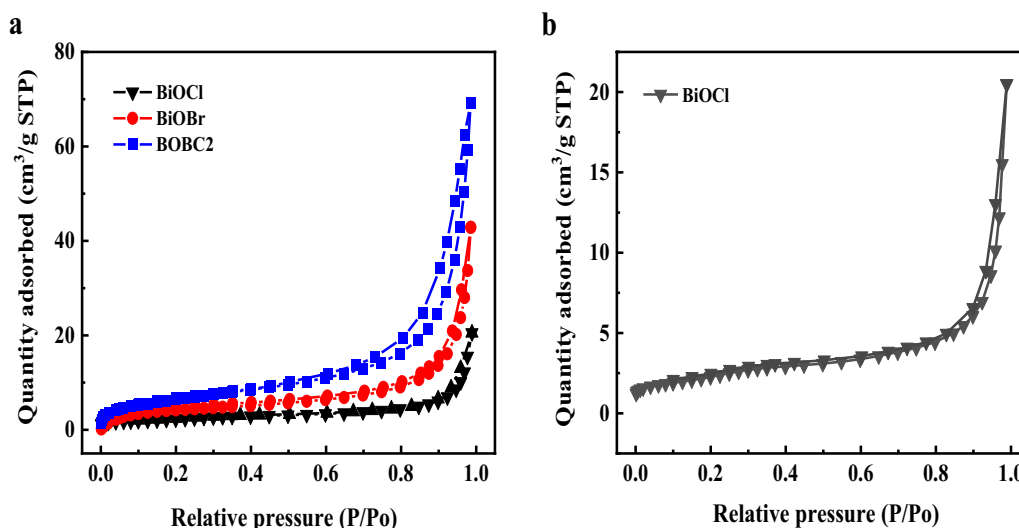


Figure 5: N₂ adsorption–desorption isotherm pore size of BiOCl, BiOBr, and BOBC2.

TABLE 1: BET-specific surface area and pore volume of BiOCl, BiOBr, and BOBC2.

Sample	BET Surface Area(m ² g ⁻¹)	Pore Volume(cm ³ g ⁻¹)
BiOCl	9.0591	0.0317
BiOBr	15.243	0.0662
BOBC2	24.471	0.1071

BOBC2. The release of energy in the form of PL emission was made while recombining electron–hole pairs. Therefore, a higher PL intensity indicates a higher rate of recombination of photogenerated charge carriers. As expected, a lower charge carrier recombination rate was found in BOBCs

compared with pure BiOBr, thus improving their photocatalytic performance [44].

The photocurrent response of pure BiOCl, BiOBr, and BOBC2 samples under visible-light (> 400 nm) illumination was tested using an electrochemical workstation. The efficiency of charge carrier separation plays a crucial role in photocatalytic reactions, and a larger photocurrent indicates higher charge carrier separation efficiency and, consequently, higher photocatalytic activity [45]. As demonstrated in the [Fig. 7(b)], the transient photocurrent responses of BiOCl, BiOBr, and BOBC2 were recorded during five on–off cycles of visible-light illumination. Figure 7(b) demonstrates that the photocurrent signal is initially low in the absence of light, then sharply increases upon illumination, and returns to its original value once the light is turned

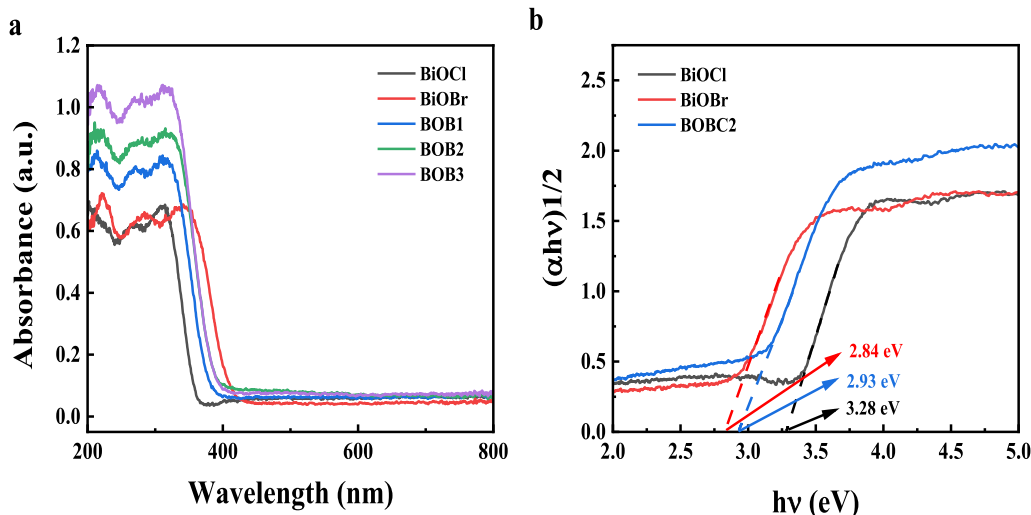


Figure 6: (a) UV–vis DRS of BiOCl, BiOBr, BOBC1, BOBC2, and BOBC3. (b) Plot of $(\alpha hv)^{1/2} - hv$ of BiOCl, BiOBr, BOBC1, BOBC2, and BOBC3.

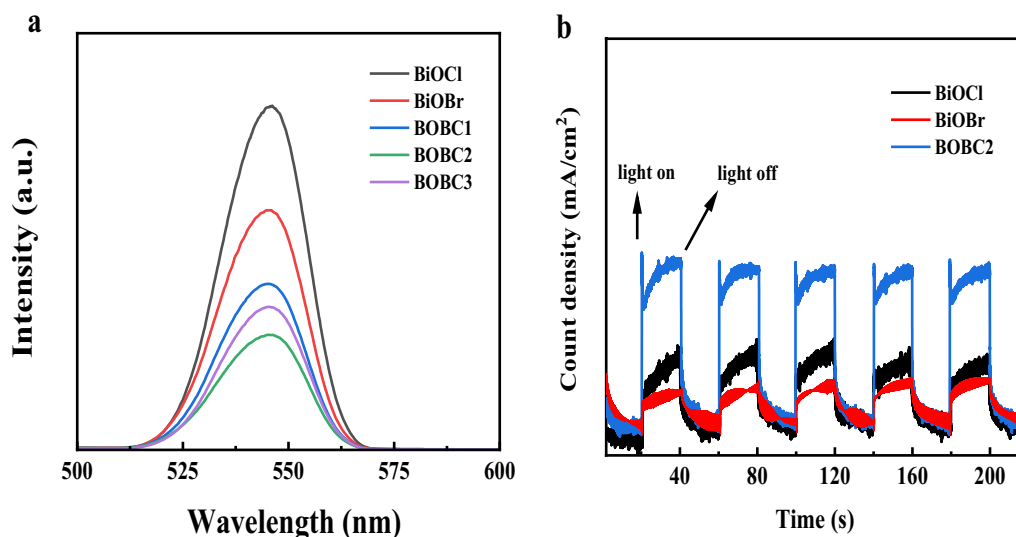


Figure 7: (a) Photoemission spectra (PL) of BiOCl, BiOBr, BOBC1, BOBC2, and BOBC3 at the excitation wavelength of 270 nm. (b) Transient photocurrent response curves of BiOCl, BiOBr, and BOBC2.

off. This behavior indicates that the photocurrent is primarily generated by light illumination on the photoanode. Compared to BiOCl and BiOBr, BOBC2 exhibits a higher transient photocurrent response under light illumination. This is attributed to the formation of heterojunctions in the BOBC2 composite material, which facilitates the migration of photogenerated charge carriers from the conduction band of BiOBr to that of BiOCl, and the migration of photogenerated holes from the valence band of BiOCl to that of BiOBr. This effective suppression of charge carrier recombination promotes charge transfer in the composite material, leading to a higher photocurrent response. These results are consistent with the findings from photoluminescence spectroscopy.

Photocatalytic tests

The performance of photocatalytic materials was evaluated using ofloxacin as the target pollutant under visible-light (> 400 nm) illumination. As depicting in [Fig. 8(a)], the absorbance of ofloxacin shows no significant change with increasing illumination time in the absence of a catalyst, indicating that ofloxacin is highly enduring and resistant to self-decomposition. After attaining the adsorption–desorption equilibrium in the solution, relation between photocatalytic degradation rates and light irradiation time were analyzed. After 100 min of illumination, the degradation rates of BiOCl, BiOBr, BOBC1, BOBC2, and BOBC3 reached 37.4%, 35%, 80.5%, 90.5%, and 82.3%, respectively. BOBCs all exhibited a higher photocatalytic degradation rate, which could be attributed to a lower recombination rate of photogenerated charge carriers because of the construction of heterojunction in the BiOCl/BiOBr composite materials [1].

The first-order kinetics of the photocatalytic degradation of the materials were analyzed by the Langmuir–Hinshelwood model (Eq. 4).

$$-\ln(C_t/C_0) = kt \quad (4)$$

In which C_0 , C_t , and k represent the peak absorbance of ofloxacin at 0 min and t minutes under light irradiation, as well as the kinetic rate constant of the catalyst, respectively.

As demonstrated in the [Fig. 8(b)], the rate constants for the photocatalytic degradation of ofloxacin using BOBCs are 0.1706 min^{-1} , 0.2406 min^{-1} , and 0.1888 min^{-1} , respectively. Among them, the BOBC2 sample exhibits the highest rate constant for ofloxacin degradation under 300 W xenon light bulb irradiation, which is approximately 5 times greater than that of pure BiOCl and pure BiOBr ($K_{\text{BiOCl}} = 0.0452$; $K_{\text{BiOBr}} = 0.0484$).

Figure 8(c) shows the change in absorbance of the ofloxacin solution during photocatalytic degradation using the BOBC2 photocatalytic material under xenon lamp irradiation. With escalating illumination time, the absorption peak of ofloxacin at 294 nm progressively decreases, indicating a reduction in the concentration of ofloxacin in the solution.

To assess the cycling stability of the BOBC2 material, four consecutive cycle tests were conducted under identical conditions. After each experiment, the solution was centrifuged and washed multiple times, subsequently undergoing drying at 60 °C for 12 h. The dried material was then ground uniformly and used for the next cycle. Figure 8(d) shows the cyclic degradation data for BOBC2. After three cycles, the degradation rate of ofloxacin using BOBC2 remains at 83.9%, indicating that BOBC2 photocatalytic material possesses a certain level of stability. As can be seen from [Fig. 8(e)], the XRD pattern of

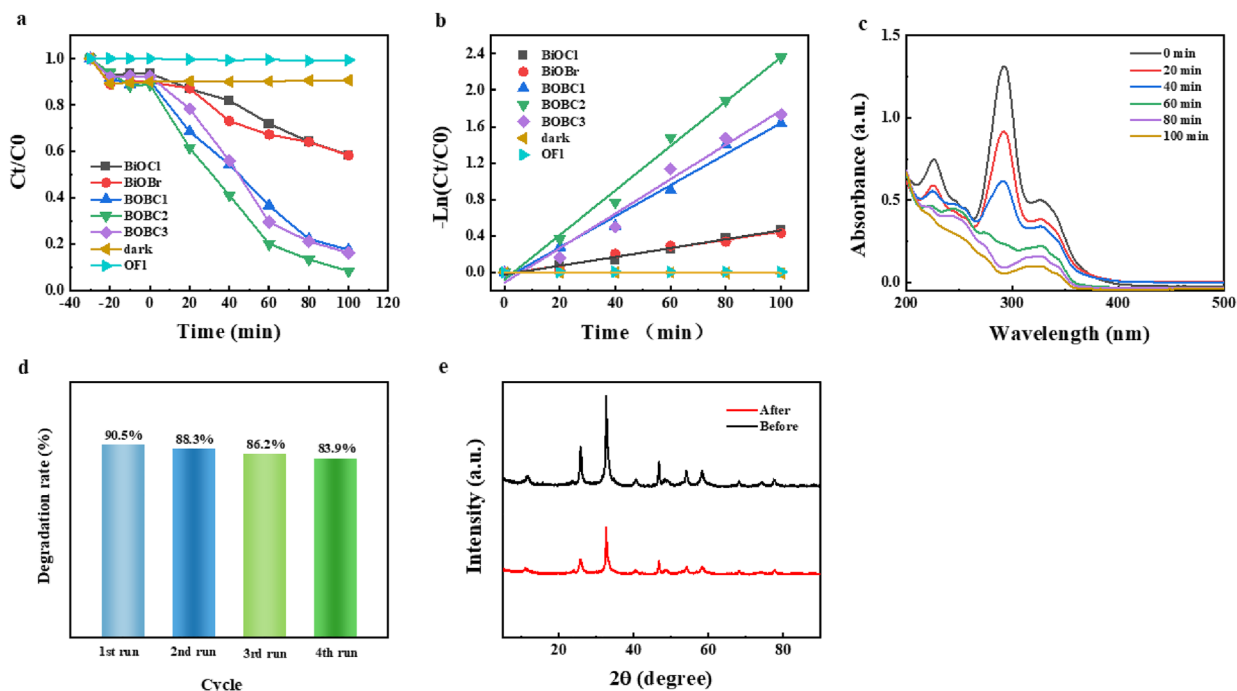


Figure 8: (a) degradation rates of ofloxacin of the samples. (b) k values of the first-order kinetic degradation rate of the samples. (c) UV-vis absorption spectra of 20 mg/L ofloxacin aqueous solution degraded by BOBC2. (d) The degradation rate of BOBC2 in four cycles, and. (e) XRD patterns of BOBC2 before and after used.

BOBC2 before and after the four cycles test, the crystal structure of BOBC2 remains unchanged after undergoing cycles test, indicating that BOBC2 may be considered as a favorable choice for the removal of ofloxacin from water due to its stability and consistent performance over multiple cycles.

Mechanism of pollutant photodegradation

Free radical capture investigations were conducted to analyze the active species engaged in the ofloxacin photocatalytic degradation process using BOBC2. Isopropanol (2 mmol L^{-1}), benzoquinone (BQ, 2 mmol L^{-1}), and ammonium oxalate (2 mmol L^{-1}) [46, 47] were employed as quenching agents to selectively capture $\cdot\text{OH}$, O_2^- , and h^+ radicals, respectively.

From [Fig. 9(a)], it can be observed that the inclusion of ammonium oxalate does not exhibit any substantial influence on the photocatalytic efficiency of BOBC2, and the degradation rate of ofloxacin decreases from 90.5 to 80%. This suggests that h^+ holes do not play a substantial role in the photocatalytic process. The inclusion of isopropanol leads to a slight decrease in the photocatalytic efficiency of BOBC2, with the degradation rate of ofloxacin decreasing from 90.5 to 57%. This indicates that $\cdot\text{OH}$ radicals play a certain role in the photocatalytic mechanism. On the other hand, the addition of BQ significantly suppresses the photocatalytic efficiency of BOBC2, with the degradation rate of ofloxacin decreasing from 90.5 to 22.7%. This demonstrates that

$\cdot\text{O}_2^-$ plays a crucial role in the photocatalytic mechanism. These findings unequivocally clearly indicate that $\cdot\text{O}_2^-$ is the primary active species during the photocatalytic degradation, while $\cdot\text{OH}$ radicals are secondary active species [19].

To further verify the active species involved in the ofloxacin photocatalytic degradation process, electron spin resonance (ESR) [48] tests were conducted. As shown in [Fig. 9(b and c)], no $\cdot\text{OH}$ and $\cdot\text{O}_2^-$ signals were detected in the dark. However, after 10 min of light irradiation, clear $\cdot\text{OH}$ and $\cdot\text{O}_2^-$ signals appeared, further confirming the presence of active free radicals $\cdot\text{OH}$ and $\cdot\text{O}_2^-$ during the reaction.

Drawing upon the experimental results mentioned above, a preliminary mechanism for the photocatalytic degradation of ofloxacin using BOBCs is proposed (Fig. 10). Under visible-light irradiation, electrons in the valence band of the semiconductor catalysts transfer to the conduction band, producing a photo-generated electron that leaves a positively charged hole in the valence band, and photoexcited electron-hole pairs are generated. The band gaps and band positions of BiOCl and BiOBr were determined utilizing the findings from UV-Vis diffuse reflectance spectroscopy (DRS) and Mulliken electronegativity theory calculations. As shown in Fig. 10, BiOBr has a lower valence band position ($E_{\text{VB BiOCl}} = 3.47 \text{ eV}$, $E_{\text{VB BiOBr}} = 3.10 \text{ eV}$) and a higher conduction band position ($E_{\text{CB BiOCl}} = 0.24 \text{ eV}$, $E_{\text{CB BiOBr}} = 0.23 \text{ eV}$) compared to BiOCl. Under the action of inner electric field in BOBC composite materials, photoexcited holes migrate from the

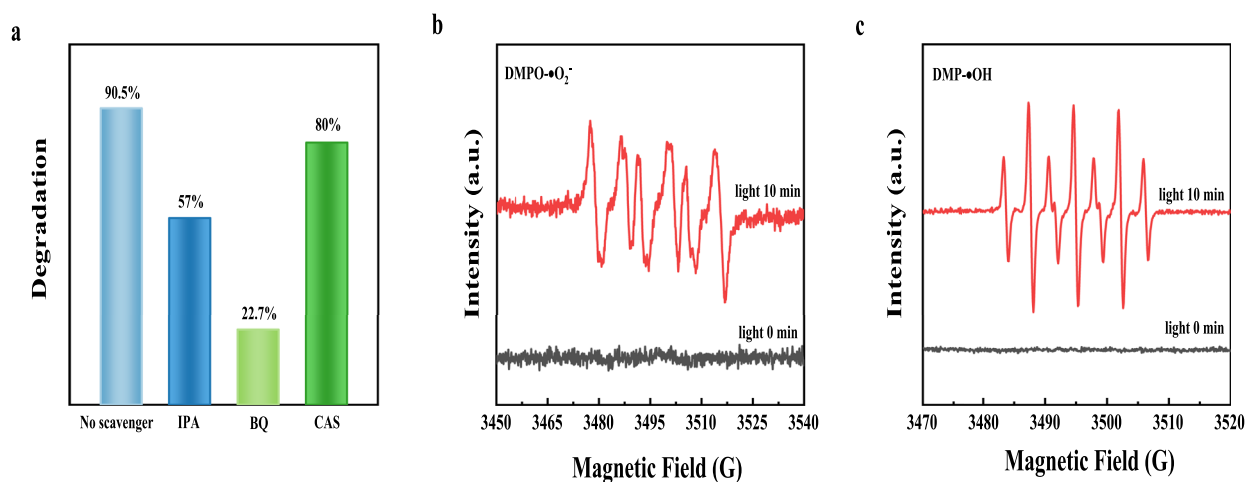


Figure 9: (a) Effects of different trapping agents on ofloxacin degradation by BOBC2. (b, c) ESR spectra of BOBC2.

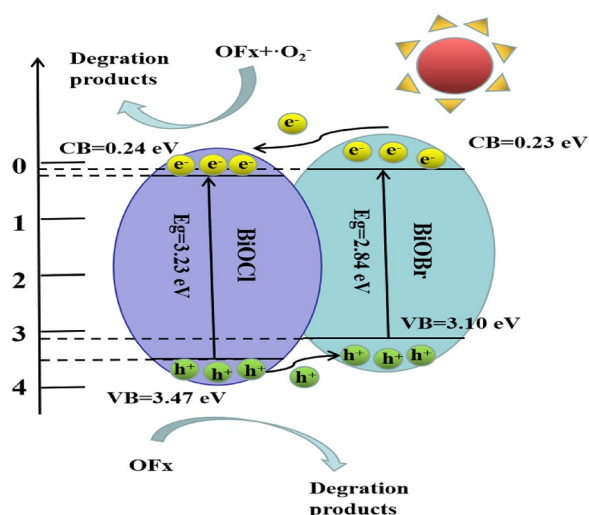


Figure 10: Photocatalytic degradation mechanism of OFI by BOBC2.

valence band position of BiOCl to that of BiOBr, where they react with OH^- to generate $\cdot\text{OH}$ radicals. Simultaneously, photoexcited electrons migrate from the conduction band position of BiOBr to that of BiOCl, where they react with $\cdot\text{O}_2^-$ adsorbed on the surface of the photocatalytic material to produce $\cdot\text{O}_2^-$ radicals [49]. Therefore, the formation of a heterojunction effectively suppresses the rapid recombination of photoinduced charge carriers, thereby enhancing the photocatalytic efficiency.

Conclusion

One-step co-precipitation method was used to prepare the flower-like BOBC composite materials with heterojunction structures. Absorption range of visible-light increases with the proportion of BiOBr increase in BOBCs compared with pure BiOCl. Compared

to pure BiOCl or BiOBr, BOBCs have a lower rate of photoinduced charge carrier recombination. The BOBC2 catalyst, with a composition ratio of 1:0.75 (BiOCl:BiOBr), exhibited the highest photocatalytic performance, achieving a 90.5% degradation rate of ofloxacin within 100 min. After three cycles testing, the degradation efficiency of ofloxacin using the BOBC2 composite material remained at 83.9%. XRD pattern of the material before and after the cycles confirmed its high chemical stability, making it favorable for practical applications.

Through quenching experiments and electron spin resonance (ESR) tests, it was confirmed that $\cdot\text{O}_2^-$ played a significant role as the active species during the photocatalytic degradation of ofloxacin, while $\cdot\text{OH}$ radicals acted as secondary active species in the photocatalytic mechanism. A reasonable mechanism for the photocatalytic degradation of ofloxacin was proposed based on these findings.

Experimental section

Materials

Bismuth nitrate pentahydrate ($\text{Bi}(\text{NO}_3)_3 \cdot 5\text{H}_2\text{O}$), potassium chloride (KCl), hexadecyl trimethyl ammonium bromide (CTAB) and acetic acid were purchased from Aladdin Biotechnology Co, Ltd. (Shanghai, China) and used in this experiment, which are analytical pure and not further purified. The pure water was obtained from the purification system in our lab.

Preparation of composite materials

Preparation of BiOCl

BiOCl was prepared by a simple precipitation method through the following process. 0.727 g of $\text{Bi}(\text{NO}_3)_3 \cdot 5\text{H}_2\text{O}$ (1.5 mmol) was dissolved in 7.5 ml of acetic acid and the solution was

denoted as solution A. 0.111 g of KCl (1.5 mmol) was dissolved in a mixture of 45 ml of pure water and 15 ml of ethylene glycol, and the solution was denoted as solution B. And then the solution B was slowly added into solution A dropwise by a magnetic stirrer at room temperature for 9 h. After stirring, the mixed solution was centrifuged at a speed of 8000 r min⁻¹ and a kind of powders was gotten. Then washed the as-prepared powders with pure water and anhydrous ethanol 5 times and dried them overnight at 70 °C to prepare the BiOCl product.

Preparation of BiOBr

The preparation process of BiOBr is the same as that of BiOCl. 0.727 g of Bi(NO₃)₃·5H₂O (1.5 mmol) was dissolved in 7.5 ml of acetic acid and the solution was, denoted as solution C. After dissolving 0.544 g (1.5 mmol) of CTAB in a mixture of 45 ml of pure water and 15 ml of ethylene glycol, which denoted as solution D, Slowly drop solution D into solution C, mix with a Magnetic stirrer for 9 h at room temperature, centrifuge the stirred solution at 8000 r min⁻¹ to obtain the product, clean the product with pure water and ethanol for many times, and dry it in an oven at 70 °C overnight to obtain BiOBr.

Preparation of BiOCl/BiOBr

BiOCl/BiOBr samples were prepared by a co-precipitation method. 0.727 g of Bi(NO₃)₃·5H₂O (1.5 mmol) was dissolved in 7.5 ml of acetic acid and the solution was denoted as solution E. A total molar mass of 1.5 mmol of KCl and CTAB (the ratio of molar of Cl: Br is 1:0.5, 1:0.75 and 1:1, respectively) was dissolved in 45 ml pure water with 15 ml ethylene glycol, and the mixed solution was referred as solution F. Slowly drop solution F into solution E by a magnetic stirrer at room temperature for 9 h. After then, the above mixed solution was centrifuged at a speed of 8000 r min⁻¹. The as-prepared powders was cleaned with pure water and ethanol multiple times, and dried in an oven at 70 °C overnight. According to the ratio of molar of Cl: Br varied from 1:0.5, 1:0.75 to 1:1, the obtained BiOCl/BiOBr samples were denoted as BOBC1, BOBC2, and BOBC3.

Photocatalyst characterization

X-ray diffraction (XRD) analysis was measured used a Cu Ka radiation source at a scanning speed of 5° min⁻¹ by a BRUKER D8 ADVANCE X-ray diffractometer. The functional groups and chemical bond of the materials were investigated with a resolution of 4 cm⁻¹ by a Fourier transform infrared spectrometer (FTIR, Thermo Scientific Nicolet iS20) in the range of wave numbers between 400 and 4000 cm⁻¹. The chemical states of the photocatalysts were analyzed by X-ray photoelectron spectroscopy (XPS, Kratos Axis Ultra DLD) with a monochromatic

Mg-Ka source operating at 20 kV. Morphologies of the catalysts were observed by a scanning electron microscopy (SEM, JEOL JSM-6700F). The surface area was calculated from N₂ absorption-desorption isotherms via Brunauer-Emmett-Teller (BET, NOVA4200e) method on a Micrometrics Micromeritics Gemini V 2380 system. A certain amount of catalyst powder was pressed onto a BaSO₄ substrate and tested using a UV vis spectrometer (UV2450, Shimadzu, Japan) to obtain the UV visible spectrum of the prepared material. A Hitachi F-4600 spectro-fluorimeter was used to record the photoluminescence (PL) spectra with an excitation wavelength of 270 nm. A Cecile 9000 UV-vis spectrophotometer was used to measure the concentration of organic pollutants. Photocurrent testing was conducted on an electrochemical workstation (CHI-660E) using a xenon lamp (300 W) as the light source. Electron Spin Resonance (ESR) experiments were carried out at room temperature using a Bruker E500 spectrometer.

Photocatalytic experiment

The concentration of ofloxacin after treated by BiOCl/BiOBr composites in different time periods was measured to evaluate their photocatalytic property. Normally, in a 40 ml of ofloxacin solution dissolve the 15 mg of photocatalyst powder (20 mg L⁻¹), which was put into the dark box for 30 min treatment to attain the adsorption-desorption equilibrium. The solution was irradiated under a 300 W xenon light bulb, and five samples were taken once every 20 min from the solution after centrifugating to remove the catalyst. The absorbance value of the supernatant was measured at the wave length of 290 nm using a UV visible spectrophotometer. After comparing the difference between the absorbance peak points before and after illumination, the photocatalytic degradation efficiency of the photocatalytic material can be calculated.

Experiments were conducted to determine the active substances involved in the photocatalytic degradation process through free radical capture. A concentration of 2 mmol L⁻¹ of benzoquinone (BQ), isopropanol (IPA), and ammonium oxalate (CAS) were added to the photocatalytic solution in the process of degradation experiments under nitrogen atmosphere, to capture hydroxyl radicals (·OH) and superoxide radicals (·O₂⁻) and hole (h⁺) quenchers, respectively. After comparing the photocatalytic degradation rate before and after adding the above active substances in order to the main active substances really participating in the photocatalytic reaction.

Cyclic experiments were tested to verify the stability of photocatalytic materials. Four cyclic tests were conducted on the photocatalytic material under the same conditions. After each cycle, the catalyst is collected by centrifugation and washing multiple times. Calculate the degradation rate for each test and compare it with the initial degradation rate.

Acknowledgments

Class III Peak Discipline of Shanghai—Materials Science and Engineering (High-Energy Beam Intelligent Processing and Green Manufacturing).

Author contributions

YZ: Writing—original draft, Investigation, Validation, Methodology, Data curation, software, Formal analysis, Writing—review & editing. WL: Conceptualization, Project administration, Writing—review & editing, Formal analysis. RG: Investigation, Conceptualization, Project administration. HL: Software, Formal analysis, Writing—original draft. YH: Investigation, Validation, Methodology.

Funding

This work was funded by Class III Peak Discipline of Shanghai—Materials Science and Engineering (High-Energy Beam Intelligent Processing and Green Manufacturing).

Data availability

All data generated or analyzed during this study are included in this published article.

Code availability

Not applicable.

Declarations

Conflict of interest The authors have no competing interests to declare that are relevant to the content of this article.

References

1. C.M. Jung, T.M. Heinze, R. Strakosha, C.A. Elkins, J.B. Sutherland, Acetylation of fluoroquinolone antimicrobial agents by an *Escherichia coli* strain isolated from a municipal wastewater treatment plant. *J. Appl. Microbiol.* **106**(2), 564–571 (2009)
2. D. Huang, J. Li, G. Zeng, W. Xue, S. Chen, Z. Li, R. Deng, Y. Yang, M. Cheng, Facile construction of hierarchical flower-like Z-scheme AgBr/Bi₂WO₆ photocatalysts for effective removal of tetracycline: degradation pathways and mechanism. *Chem. Eng. J.* **375**, 121991 (2019)
3. R. Jiang, G. Lu, Z. Yan, D. Wu, R. Zhou, X. Bao, Insights into a CQD-SnNb₂O₆/BiOCl Z-scheme system for the degradation of benzocaine: influence factors, intermediate toxicity and photocatalytic mechanism. *Chem. Eng. J.* **374**, 79–90 (2019)
4. D. Díez-del-Molino, E. García-Berthou, R.M. Araguas, C. Alcaraz, O. Vidal, N. Sanz, J.L. García-Marín, Insights into a CQD-SnNb₂O₆/BiOCl Z-scheme system for the degradation of benzocaine: influence factors, intermediate toxicity and photocatalytic mechanism. *Sci. Total Environ.* **637**, 1372–1382 (2018)
5. Y. Qi, J. Li, Y. Zhang, Q. Cao, Y. Si, Z. Wu, M. Akram, X. Xu, Novel lignin-based single atom catalysts as peroxymonosulfate activator for pollutants degradation: role of single cobalt and electron transfer pathway. *Appl. Catal. B* **286**, 119910 (2021)
6. J. Xue, S. Ma, Y. Zhou, Z. Zhang, M. He, Facile photochemical synthesis of Au/Pt/g-C₃N₄ with plasmon-enhanced photocatalytic activity for antibiotic degradation. *ACS Appl. Mater. Interfaces* **7**(18), 9630–9637 (2015)
7. T. Paul, M.C. Dodd, T.J. Strathmann, Photolytic and photocatalytic decomposition of aqueous ciprofloxacin: transformation products and residual antibacterial activity. *Water Res.* **44**(10), 3121–3132 (2010)
8. S. Castiglioni, R. Bagnati, R. Fanelli, F. Pomati, D. Calamari, E. Zuccato, Removal of pharmaceuticals in sewage treatment plants in Italy. *Environ. Sci. Technol.* **40**(1), 357–363 (2006)
9. Z. Zhu, P. Huo, Z. Lu, Y. Yan, Z. Liu, W. Shi, C. Li, H. Dong, Fabrication of magnetically recoverable photocatalysts using g-C₃N₄ for effective separation of charge carriers through like-Z-scheme mechanism with Fe₃O₄ mediator. *Chem. Eng. J.* **331**, 615–625 (2018)
10. W. Zhang, F. Bi, Y. Yu, H. He, Phosphoric acid treating of ZSM-5 zeolite for the enhanced photocatalytic activity of TiO₂/HZSM-5. *J. Mol. Catal. A: Chem.* **372**, 6–12 (2013)
11. Z. Li, M. Qi, C. Tu, W. Wang, J. Chen, A.J. Wang, Highly efficient removal of chlorotetracycline from aqueous solution using graphene oxide/TiO₂ composite: properties and mechanism. *Appl. Surf. Sci.* **425**, 765–775 (2017)
12. Y. Wu, F. Xu, D. Guo, Z. Gao, D. Wu, K. Jiang, Synthesis of ZnO/CdSe hierarchical heterostructure with improved visible photocatalytic efficiency. *Appl. Surf. Sci.* **274**, 39–44 (2013)
13. Y. Guo, J. Zhang, D. Zhou, S. Dong, Fabrication of Ag/CDots/BiOBr ternary photocatalyst with enhanced visible-light driven photocatalytic activity for 4-chlorophenol degradation. *J. Mol. Liq.* **262**, 194–203 (2018)
14. X.J. Guo, M. Zhen, H. Liu, L. Liu, BiOBr–BiOI microsphere assembled with atom-thick ultrathin nanosheets and its high photocatalytic activity. *RSC Adv.* **5**(31), 24777–24782 (2015)
15. R.B. Arthur, J.C. Ahern, H.H. Patterson, Application of BiOX photocatalysts in remediation of persistent organic pollutants. *Catalysts* **8**(12), 604 (2018)
16. S. Zhao, Y. Zhang, Y. Zhou, K. Qiu, C. Zhang, J. Fang, X. Sheng, Reactable polyelectrolyte-assisted preparation of flower-like Ag/AgCl/BiOCl composite with enhanced photocatalytic activity. *J. Photochem. Photobiol. A* **350**, 94–102 (2018)
17. J. Cai, Y. Xie, C. Ma, X. Wang, L. Wang, P. Ning, Y. Ma, rGO-modified BiOX (X = Cl, I, Br) for enhanced photocatalytic eradication of gaseous mercury. *Appl. Surf. Sci.* **594**, 153502 (2022)
18. J. Li, Y. Liu, Y. Zhou, S. Liu, Y. Liang, T. Luo, G. Dai, Enhanced visible-light photocatalytic activity of Bi₂O₂CO₃ nanoplates by

- Fe-doping in the degradation of rhodamine B. *Mater. Res. Bull.* **107**, 438–445 (2018)
19. X. Li, J. Xiong, X. Gao, J. Ma, Z. Chen, B. Kang, J. Liu, H. Li, Z. Feng, J. Huang, Novel BP/BiOBr S-scheme nano-heterojunction for enhanced visible-light photocatalytic tetracycline removal and oxygen evolution activity. *J. Hazard. Mater.* **387**, 121690 (2020)
 20. J. Mei, Y. Tao, C. Gao, Q. Zhu, H. Zhang, J. Yu, Z. Fang, H. Xu, Y. Wang, G. Li, Photo-induced dye-sensitized BiPO₄/BiOCl system for stably treating persistent organic pollutants. *Appl. Catal. B* **285**, 119841 (2021)
 21. J. Zhang, J. Xia, S. Yin, H. Li, H. Xu, M. He, L. Huang, Q. Zhang, Improvement of visible-light photocatalytic activity over flower-like BiOCl/BiOBr microspheres synthesized by reactable ionic liquids. *Colloids Surf. A* **420**, 89–95 (2013)
 22. S.M. Aghdam, M. Haghighi, S. Allahyari, L. Yosefi, Precipitation dispersion of various ratios of BiOI/BiOCl nanocomposite over g-C₃N₄ for promoted visible-light nanophotocatalyst used in removal of acid orange 7 from water. *J. Photochem. Photobiol. A* **338**, 201–212 (2017)
 23. Z. Liu, H. Ran, B. Wu, P. Feng, Y. Zhu, Synthesis and characterization of BiOI/BiOBr heterostructure films with enhanced visible-light photocatalytic activity. *Colloids Surf. A* **452**, 109–114 (2014)
 24. S. Zhang, J. Yang, Microwave-assisted synthesis of BiOCl/BiOBr composites with improved visible-light photocatalytic activity. *Ind. Eng. Chem. Res.* **54**(41), 9913–9919 (2015)
 25. X. Xiao, R. Hao, M. Liang, X. Zuo, J. Nan, L. Li, W. Zhang, One-pot solvothermal synthesis of three-dimensional (3D) BiOI/BiOCl composites with enhanced visible-light photocatalytic activities for the degradation of bisphenol-A. *J. Hazard. Mater.* **233**, 122–130 (2012)
 26. H. Liao, J. Zhong, J. Li, S. Huang, R. Duan, Photocatalytic properties of flower-like BiOBr/BiOCl heterojunctions in-situ constructed by a reactable ionic liquid. *Inorg. Chem. Commun.* **134**, 109063 (2021)
 27. G. Liu, H. Xu, D. Li, Z. Zou, Q. Li, D. Xia, BiOCl/BiOBr heterojunction with rich oxygen vacancies induced by ultraviolet and its enhanced photocatalytic performance. *Eur. J. Inorg. Chem.* **2019**(46), 4887–4893 (2019)
 28. X. Jia, J. Cao, H. Lin, M. Zhang, X. Guo, S. Chen, Transforming type-I to type-II heterostructure photocatalyst via energy band engineering: a case study of I-BiOCl/I-BiOBr. *Appl. Catal. B* **204**, 505–514 (2017)
 29. H.T. Wang, M.S. Shi, H.F. Yang, N. Chang, H. Zhang, Y.P. Liu, M.C. Lu, D. An, D.Q. Chu, Transforming type-I to type-II heterostructure photocatalyst via energy band engineering: a case study of I-BiOCl/I-BiOBr. *Mater. Lett.* **222**, 164–167 (2018)
 30. L. Ye, J. Liu, Z. Jiang, T. Peng, L. Zan, Transforming type-I to type-II heterostructure photocatalyst via energy band engineering: a case study of I-BiOCl/I-BiOBr. *Appl. Catal. B* **142**, 1–7 (2013)
 31. W. Li, Y. Zou, X. Geng, F. Xiao, G. An, D. Wang, Constructing highly catalytic oxidation over BiOBr-based hierarchical microspheres: importance of redox potential of doped cations. *Mol. Catal.* **438**, 19–29 (2017)
 32. X. Gao, W. Peng, G. Tang, Q. Guo, Y. Luo, Highly efficient and visible-light-driven BiOCl for photocatalytic degradation of carbamazepine. *J. Alloy. Compd.* **757**, 455–465 (2018)
 33. J. Liu, Y. Luan, C. An, J. Zhang, D. Wang, Y. Li, Silver iodide nanospheres wrapped in reduced graphene oxide for enhanced photocatalysis. *ChemCatChem* **7**(18), 2918–2923 (2015)
 34. F. Qiu, W. Li, F. Wang, H. Li, X. Liu, C. Ren, Preparation of novel pn heterojunction Bi₂O₂CO₃/BiOBr photocatalysts with enhanced visible-light photocatalytic activity. *Colloids Surf. A* **517**, 25–32 (2017)
 35. J. Di, J. Xia, M. Ji, B. Wang, S. Yin, Q. Zhang, Z. Chen, H. Li, Carbon quantum dots modified BiOCl ultrathin nanosheets with enhanced molecular oxygen activation ability for broad spectrum photocatalytic properties and mechanism insight. *ACS Appl. Mater. Interfaces.* **7**(36), 20111–20123 (2015)
 36. H. Liu, Y. Su, Z. Chen, Z. Jin, Y. Wang, Graphene sheets grafted three-dimensional BiOBr_{0.2}I_{0.8} microspheres with excellent photocatalytic activity under visible-light. *J. Hazard. Mater.* **266**, 75–83 (2014)
 37. Q. Hu, M. Ji, J. Di, B. Wang, J. Xia, Y. Zhao, H. Li, Ionic liquid-induced double regulation of carbon quantum dots modified bismuth oxychloride/bismuth oxybromide nanosheets with enhanced visible-light photocatalytic activity. *J. Colloid Interface Sci.* **519**, 263–272 (2018)
 38. Q. Wang, J. Huang, H. Sun, K.Q. Zhang, Y. Lai, Uniform carbon dots@TiO₂ nanotube arrays with full spectrum wavelength light activation for efficient dye degradation and overall water splitting. *Nanoscale* **9**(41), 16046–16058 (2018)
 39. T.B. Li, G. Chen, C. Zhou, Z.Y. Shen, R.C. Jin, J.X. Sun, New photocatalyst BiOCl/BiOI composites with highly enhanced visible-light photocatalytic performances. *Dalton Trans.* **40**(25), 6751–6758 (2011)
 40. X. He, F. Deng, T. Shen, L. Yang, D. Chen, J. Luo, X. Luo, X. Min, F. Wang, Exceptional adsorption of arsenic by zirconium metal-organic frameworks: engineering exploration and mechanism insight. *J. Colloid Interface Sci.* **539**, 223–234 (2019)
 41. J. Xia, S. Yin, H. Li, H. Xu, L. Xu, Y. Xu, Improved visible-light photocatalytic activity of sphere-like BiOBr hollow and porous structures synthesized via a reactable ionic liquid. *Dalton Trans.* **40**(19), 5249–5258 (2011)
 42. L. Ye, J. Liu, C. Gong, L. Tian, T. Peng, L. Zan, Two different roles of metallic Ag on Ag/AgX/BiOX (X = Cl, Br) visible-light photocatalysts: surface plasmon resonance and Z-scheme bridge. *ACS Catal.* **2**(8), 1677–1683 (2012)

43. J. Wang, L. Tang, G. Zeng, Y. Deng, H. Dong, Y. Liu, L. Wang, B. Peng, C. Zhang, F. Chen, F. Chen, 0D/2D interface engineering of carbon quantum dots modified Bi_2WO_6 ultrathin nanosheets with enhanced photoactivity for full spectrum light utilization and mechanism insight. *Appl. Catal. B* **222**, 115–123 (2018)
44. Y.J. Sun, J.Y. He, D. Zhang, X.J. Wang, J. Zhao, R.H. Liu, F.T. Li, Simultaneous construction of dual-site phosphorus modified g- C_3N_4 and its synergistic mechanism for enhanced visible-light photocatalytic hydrogen evolution. *Appl. Surf. Sci.* **517**, 146192 (2020)
45. Q. Xiang, J. Yu, M. Jaroniec, Preparation and enhanced visible-light photocatalytic H_2 -production activity of graphene/ C_3N_4 composites. *J. Phys. Chem. C* **115**(15), 7355–7363 (2011)
46. Z. Jia, T. Li, Z. Zheng, J. Zhang, J. Liu, R. Li, Y. Wang, X. Zhang, Y. Wang, C. Fan, Preparation and enhanced visible-light photocatalytic H_2 -production activity of graphene/ C_3N_4 composites. *Chem. Eng. J.* **380**, 122422 (2020)
47. D. Ma, J. Zhong, R. Peng, J. Li, R. Duan, Effective photoinduced charge separation and photocatalytic activity of hierarchical microsphere-like C60/BiOCl . *Appl. Surf. Sci.* **465**, 249–258 (2019)
48. Y. Lv, Y. Zhu, Y. Zhu, Enhanced photocatalytic performance for the BiPO_{4-x} nanorod induced by surface oxygen vacancy. *J. Phys. Chem. C* **117**(36), 18520–18528 (2013)
49. S. Jonjana, A. Phuruangrat, S. Thongtem, O. Wiranwetchayan, T. Thongtem, Preparation and characterization of $\text{Ag}_3\text{VO}_4/\text{Bi}_2\text{MoO}_6$ nanocomposites with highly visible-light-induced photocatalytic properties. *Mater. Lett.* **180**, 93–96 (2016)

Publisher's Note Springer Nature remains neutral with regard to jurisdictional claims in published maps and institutional affiliations.

Springer Nature or its licensor (e.g. a society or other partner) holds exclusive rights to this article under a publishing agreement with the author(s) or other rightsholder(s); author self-archiving of the accepted manuscript version of this article is solely governed by the terms of such publishing agreement and applicable law.